Arctic amplification–induced decline in West and South Asia dust warrants stronger antidesertification toward carbon neutrality

Fan Wang[a,b] (ID), Yangyang Xu[c,d] (ID), Piyushkumar N. Patel[e,f] (ID), Ritesh Gautam[d], Meng Gao[a,b,1] (ID), Cheng Liu[g,h,1], Yihui Ding[i], Haishan Chen[i] (ID), Yuanjian Yang[i], Yuyu Zhou[k], Gregory R. Carmichael[i] (ID), and Michael B. McElroy[b] (ID)

Dust loading in West and South Asia has been a major environmental issue due to its negative effects on air quality, food security, energy supply and public health, as well as on regional and global weather and climate. Yet a robust understanding of its recent changes and future projection remains unclear. On the basis of several high-quality remote sensing products, we detect a consistently decreasing trend of dust loading in West and South Asia over the last two decades. In contrast to previous studies emphasizing the role of local land use changes, here, we attribute the regional dust decline to the continuous intensification of Arctic amplification driven by anthropogenic global warming. Arctic amplification results in anomalous mid-latitude atmospheric circulation, particularly a deepened trough stretching from West Siberia to Northeast India, which inhibits both dust emissions and their downstream transports. Large ensemble climate model simulations further support the dominant role of greenhouse gases induced Arctic amplification in modulating dust loading over West and South Asia. Future projections under different emission scenarios imply potential adverse effects of carbon neutrality in leading to higher regional dust loading and thus highlight the importance of stronger anti-desertification counter-actions such as reforestation and irrigation management.

aerosols | climate change | atmospheric circulation | decarbonization

Dust aerosol is a suspension of tiny mineral particles in the atmosphere. This is the most abundant aerosol by mass in the atmosphere and constitutes more than 50% of the global aerosol loading (1, 2). Dust is often mixed with high salt, bacteria, and metal contents, making it toxic for people and plants (3–5). Dust is also critical in global biogeochemical cycles, acting as a potential source of iron for marine ecosystems (6). West and South Asia are known to frequently experience high levels of dust pollution especially during pre-monsoon season (7–9). High dust loading in these regions imposes negative impacts on the hydrological cycle, food security, solar energy production, and human health (10–13). For example, the Economic and Social Commission for Asia and the Pacific (14) reported that sand and dust storms led to more than 500 million people in India exposed to medium and high levels of poor air quality and over 107 million dollars in economic losses in 2019 alone. Giannadaki et al. (15) reported hundreds of thousands of cardio-pulmonary and lung cancer mortalities due to dust exposure in West Asia. Apart from the direct impacts on ecosystem and public health, dust aerosols scatter and absorb solar radiation, and act as natural seeds for cirrus clouds in the upper troposphere, affecting regional and global weather and climate (16–18). Kok et al. (19) highlighted a cooling effect of dust on global climate through the radiative effect estimated to be -0.2 ± 0.5 W m^{-2}. For monsoon regions such as West and South Asia, dust radiative effects are found to regulate surface energy balance and modulate monsoon duration and intensity of precipitation (20–22).

High dust levels in West and South Asia are mainly due to strong local emission and long-distance transport (23, 24). The dust emissions are highly sensitive to local conditions such as surface winds and soil moisture (25). The Arabian Peninsula and Tigris-Euphrates alluvial plain are prime emission sources in the Middle East, and the Thar Desert and the Indo-Gangetic Plain (IGP) are major sources of dust in the Indian subcontinent, collectively contributing to about 20% of global dust emission (24, 26–28). Strong northwesterly winds forced by a wave of high pressure that funnels through the Persian Gulf between Saudi Arabia and Iran results in persistent sand and dust storms in West Asia in the spring and summer months (29). Due to extremely dry conditions and strong winds, 5 to 10 dust storms are generated annually over the Thar Desert and strike northwest India during the pre-monsoon season (30). Dust transported from the Northern Africa partially contributes to the high level of dust loading in West Asia and dust originating from the Middle

Significance

Excessive dust loading threats public health and food security and affects regional and global climate. This study reveals a robust and significant decrease in dust loading across West and South Asia in recent decades, and attributes the long-term trend to the Arctic amplification induced circulation changes due to anthropogenic global warming. These findings raise awareness of potential challenges related to increasing dust loading in this region with global efforts to reach carbon neutrality and thus underscore the importance of local land-based anti-desertification measures in concert with broad climate mitigation strategies.

East and the northeast Africa is another important source of dust in South Asia (31). Dust generated from the arid and semi-arid regions in the Middle East can be transported thousands of kilometers from West Asia to northern India by the prevailing westerly winds (29, 32).

Large-scale atmospheric circulation is the key driving force that affects local emission conditions as well as the long-range transport processes of dust aerosols in West and South Asia. The mid-latitude circulation pattern is subject to the influence of major climate modes (directly or indirectly via teleconnection), such as sudden stratospheric warming, Arctic ice loss, el niño/southern oscillation (ENSO), and the Indian ocean dipole (IOD) (33–35). Changes in large-scale circulation directly modify the direction and magnitude of long-distance dust transport (25, 36), and also regulate emission processes by affecting regional precipitation, soil moisture and near-surface wind speed, and boundary-layer stability (37, 38). For example, cooling in the Tibetan Plateau in conjunction with warming in the Southern India was shown to generate easterly wind anomalies, suppressing local dust emissions and dust transport from the Middle East and Sahara to India (39). Dust emissions in the Middle East, Southwest Asia, and the western Sahel were strongly influenced by the IOD through its impact on local rainfall and the shamal winds (i.e., northwesterly wind blowing over Iraq and the Persian Gulf) (37, 40). Global climate has undergone significant changes in recent decades due to anthropogenic emission of greenhouse gases (GHG) and other pollutants (41, 42). Anthropogenic climate change imposed perturbation on atmospheric circulation and monsoon rainfall patterns in West and South Asia (43–45). It is thus imperative to thoroughly analyze its subsequent impacts on the emission and transport processes of dust over these regions (depicted in *SI Appendix*, Fig. S1A).

Using satellite retrievals, reanalysis, and surface observations, a majority of previous studies have reported declining trends in dust loading across West and South Asia (44, 46–49), although some studies have suggested increasing (50) or even reversing (51) trends over the past two decades. In this study, we adopted three high-quality satellite retrieval products to detect a consistently long-term decrease in dust loading over the broader region of West and South Asia in the last two decades (up to 2019). We truncated the time period to 2019, as reduced anthropogenic emissions in COVID-19 (especially in 2020) were suggested to perturb atmospheric circulation and rainfall patterns which could influence dust loading in this region (39, 52). These three products, including the infrared atmospheric sounder interferometer (IASI) dust optical depth (DOD), the cloud-aerosol lidar with orthogonal polarization (CALIOP) DOD, and the moderate resolution imaging spectroradiometer (MODIS) aerosol optical depth (AOD), feature high reliability, benefiting from well-established instruments, rigorous validation procedures, and broad scientific assessment (53–57). Tindan et al. (58) reported better performance in DOD retrieval using IASI compared to CALIOP because of stronger aerosol-cloud discrimination capabilities. Therefore, in this study, we use the IASI DOD as the primary dataset for detection of the recent trends in dust loading, while CALIOP DOD and MODIS AOD are presented as supporting data.

Previous studies have primarily attributed the decline in dust loading in West and South Asia to increased regional rainfall and suppressed emissions (44, 46), potentially driven by a local greening due to irrigation expansion (47, 49). However, we contend that there may be more influential contributors at the global scale to this widespread decrease in dust loading across such extensive spatial domains. Using the reanalysis products and historical model simulations from the coupled model intercomparison project phase 6 (CMIP6), we attributed the recent decline in dust

loading to the Arctic amplification–related mid-latitude circulation changes. Large ensemble model simulations were used to further support the dominant role of GHG-induced Arctic amplification in modulating dust loading, rather than natural variability or local land use changes. Future shifts in dust loading in West and South Asia under different shared socioeconomic pathway (SSP) scenarios were also evaluated, showing an increase in dust loading under the more aggressively mitigated scenarios. Our results raise awareness for potential dust loading enhancement in West and South Asia toward a low carbon future, highlighting the need to strengthen local anti-desertification efforts as part of the broader climate mitigation strategies.

Results

Decreased Dust Loading in West and South Asia. Desert dust sources in West and South Asia are mainly concentrated in the border regions of India and Pakistan, and the Arabian Peninsula (*SI Appendix*, Fig. S1A), whereas the transport of dust aerosols and severe dust outbreaks are frequently observed across west Asia and northern parts of south Asia in particular over the Indo-Gangetic Plains (*SI Appendix*, Fig. S1B). From 2008 to 2019, DOD over most parts of West and South Asia experienced decreasing trends, with the largest decline found in the IGP and the Persian Gulf Coast regions, and DOD over the Middle East also shows remarkable declines (Fig. 1A). The DOD over the entire land region decreased significantly at an area-averaged rate of –0.0036 per year (–2.88%/year, $P < 0.01$) (Fig. 1 C and E). There was an unusual enhancement of DOD in 2018 due to anomalous easterlies and droughts in the pre-monsoon seasons of South Asia (30). To verify the robustness of the changes, we divided the entire study period into two subperiods: Pre-period (2008 to 2013) and Post-period (2014 to 2019). In most parts of South Asia, DOD is at least 0.05 (50%) lower in the Post-period compared to the Pre-period (Fig. 1B). Notably, DOD over Iraq can be 0.1 (75%) smaller in the Post-period than in the Pre-period. DOD over the oceans surrounding the Arabian Peninsula exhibits more significant decreasing trends with a spatially averaged rate of –0.0038 per year (–4.20%/year, $P < 0.01$) (Fig. 1 D and F).

Retrievals from MODIS also support decreasing trends in dust loading in West and South Asia (Fig. 2), consistent with the trend detected in the IASI DOD product. Although the MODIS AOD includes contributions from all aerosol types, the aerosol loading is dominated by dust during the May–July pre-monsoon season over the source and transport regions in West and South Asia as represented in four boxes shown in Fig. 2A. The time series depict a general decline over the longer 2003 to 2019, indicating the trend over 2008 to 2019 detected in IASI DOD is not due to the spurious anomaly of 2008. The CALIOP DOD also shows a declining trend since 2007 (Fig. 2 G–I), consistently in daytime and nighttime records as well as the surface and mid-troposphere. At higher troposphere, percentage change in dust occurrence frequency (DOF) exhibits positive values, which is associated with increased upward movement of air from Pre-period to Post-period. Total and coarse mode AOD in most sites of the Aerosol Robotic Network (AERONET) also show decreasing trends in West and South Asia over the study period (Fig. 2K and *SI Appendix*, Fig. S1H). The decreasing rates inferred from IASI DOD and AERONET AOD are generally consistent (Fig. 2L).

DOD Decline Due to Global Warming Induced Arctic Amplification. Fig. 3A shows that most regions in Europe, North Africa, West Asia, and South Asia have experienced warming in the Post-period compared to the Pre-period. Moreover, the
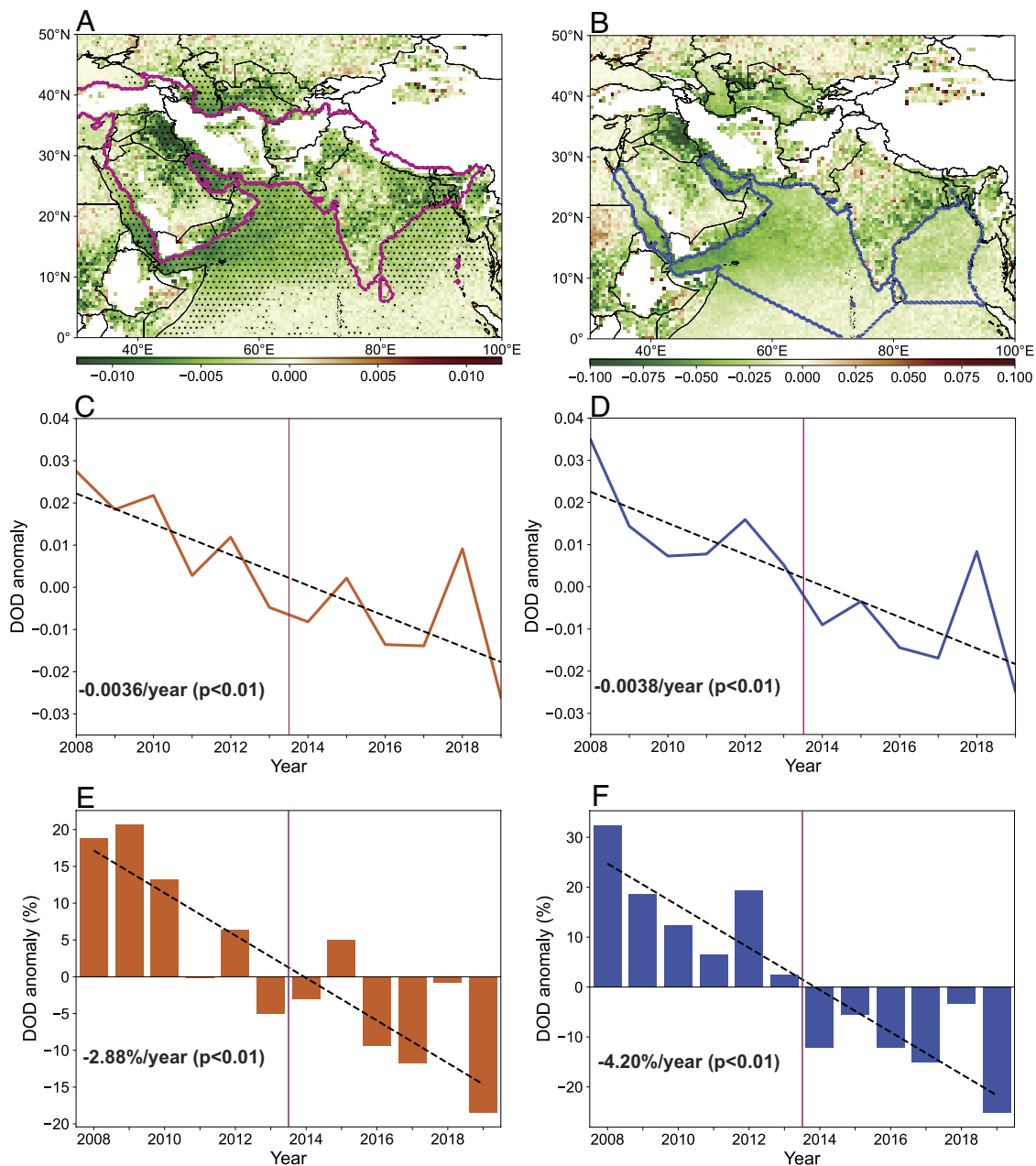
Fig. 1. Temporal variations of DOD. (*A*) Spatial distribution of DOD trend (1 per year) from 2008 to 2019. Black dots denote areas with significant trend ($P < 0.05$). (*B*) Spatial distribution of changes of DOD from the Pre-period (2008 to 2013) to the Post-period (2014 to 2019) period. Whited-out areas in (*A* and *B*) are plateau regions with missing data. The spatial distributions of DOD changes in percentage are shown in *SI Appendix*, Fig. S1 *C* and *D*. (*C*) Time series of spatially averaged DOD anomalies over West and South Asia (land regions enclosed by purple dashed lines in *A*). (*D*) Time series of spatially averaged DOD anomalies over Northern India Ocean (ocean regions enclosed by blue dashed lines in *B*, including the Red Sea, the Gulf of Aden, the Arabian Sea, the Gulf of Oman, the Persian Gulf, the Laccadive Sea and the Bay of Bengal). (*E*) Time series of percentage changes of spatially averaged DOD anomalies over West and South Asia lands as in (*A*). (*F*) Time series of percentage changes of spatially averaged DOD anomalies over the oceans around West and South Asia as in (*B*).

Arctic is warming at a faster rate than the rest of the planet, a phenomenon well known as Arctic amplification (59). We quantify the variation of Arctic amplification intensity (AAI) from 2008 to 2019 by calculating differences in the annual average surface temperature anomalies between the pan-Arctic (60° to 90°N) and the entire northern hemisphere (0° to 90°N) [(60), Fig. 3*B*]. We note a general increase in AAI over 2008 to 2019, which reduces the thermal contrast between the Arctic and the Northern Hemisphere. AAI has been documented to have been increasing since the center of the second half of the 20th century and has become more pronounced after 2000 (43, 61–64). As a result, Arctic amplification exerts profound

impacts on the mid-latitude circulation pattern by perturbing storm tracks, the position and structure of the jet stream, and planetary wave activity (43, 65). The correlation coefficient (R) between Arctic-NH thermal contrast and dust loading in West and South Asia is found to be as high as 0.77 ($P < 0.01$), which is indicative that the decline in dust loading over West and South Asia may have a potential connection with the reduced Arctic-NH thermal contrast. We also explored potential impacts of other meteorological oscillations, including El Niño/La Niña, madden-julian oscillation (MJO), India ocean dipole (IOD), and Arctic oscillation (AO) (*SI Appendix*, Fig. S2). However, none of them matched the trends of dust over 2008 to 2019.
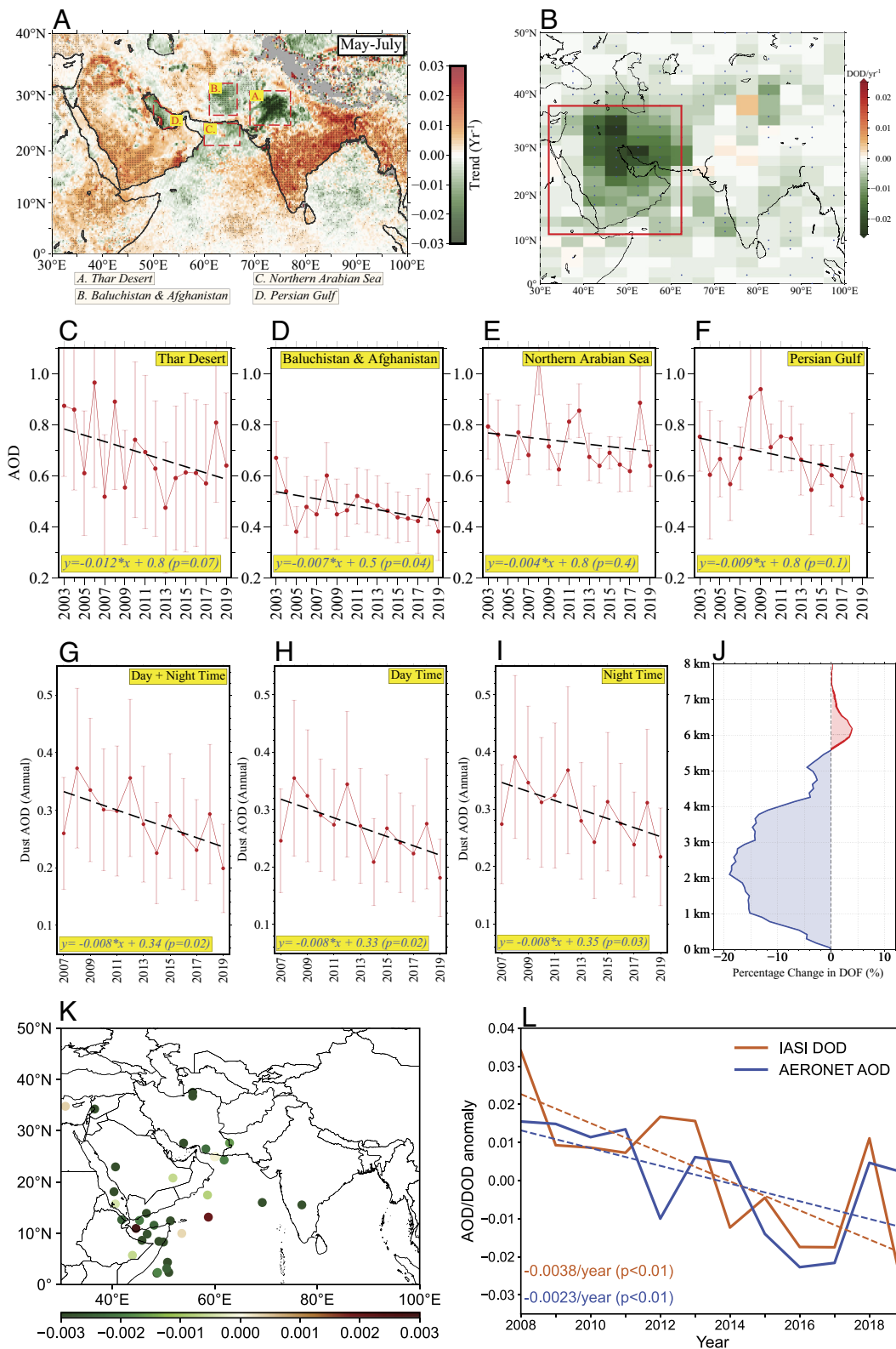
Fig. 2. Temporal variations of MODIS AOD, CALIOP DOD, and AERONET AOD. (*A*) Spatial distribution of MODIS AOD trend (1 per year) from 2003 to 2019. Black dots denote areas with significant trends (*P* < 0.05). (*B*) Spatial distribution of CALIOP DOD trend (1 per year) from 2007 to 2019. Black dots denote areas with significant trends (*P* < 0.05). Time series of spatially averaged MODIS AOD over the Thar Desert (*C*), Baluchistan & Afghanistan (*D*), Northern Arabian Sea (*E*), and Persian Gulf (*F*) during May to July from 2003 to 2019. Time series of spatially averaged daily (*G*), daytime (*H*), and nighttime (*I*) CALIOP DOD over the Middle East (12°N to 38°N, 32°E to 62°E, red box in *B*) from 2007 to 2019. (*J*) Percentage decrease in DOF (calculated using CALIPSO dust profiles) over the Middle East (red square in *B*, original CALIPSO orbit tracks are shown in *SI Appendix*, Fig. S18) from the first 3 y (2007 to 2009) to the last 3 y (2017 to 2019). (*K*) Spatial distribution of AERONET AOD trend (1 per year) from 2008 to 2019. (*L*) Time series of AERONET AOD and IASI DOD anomalies at AERONET sites over West and South Asia from 2008 to 2019.
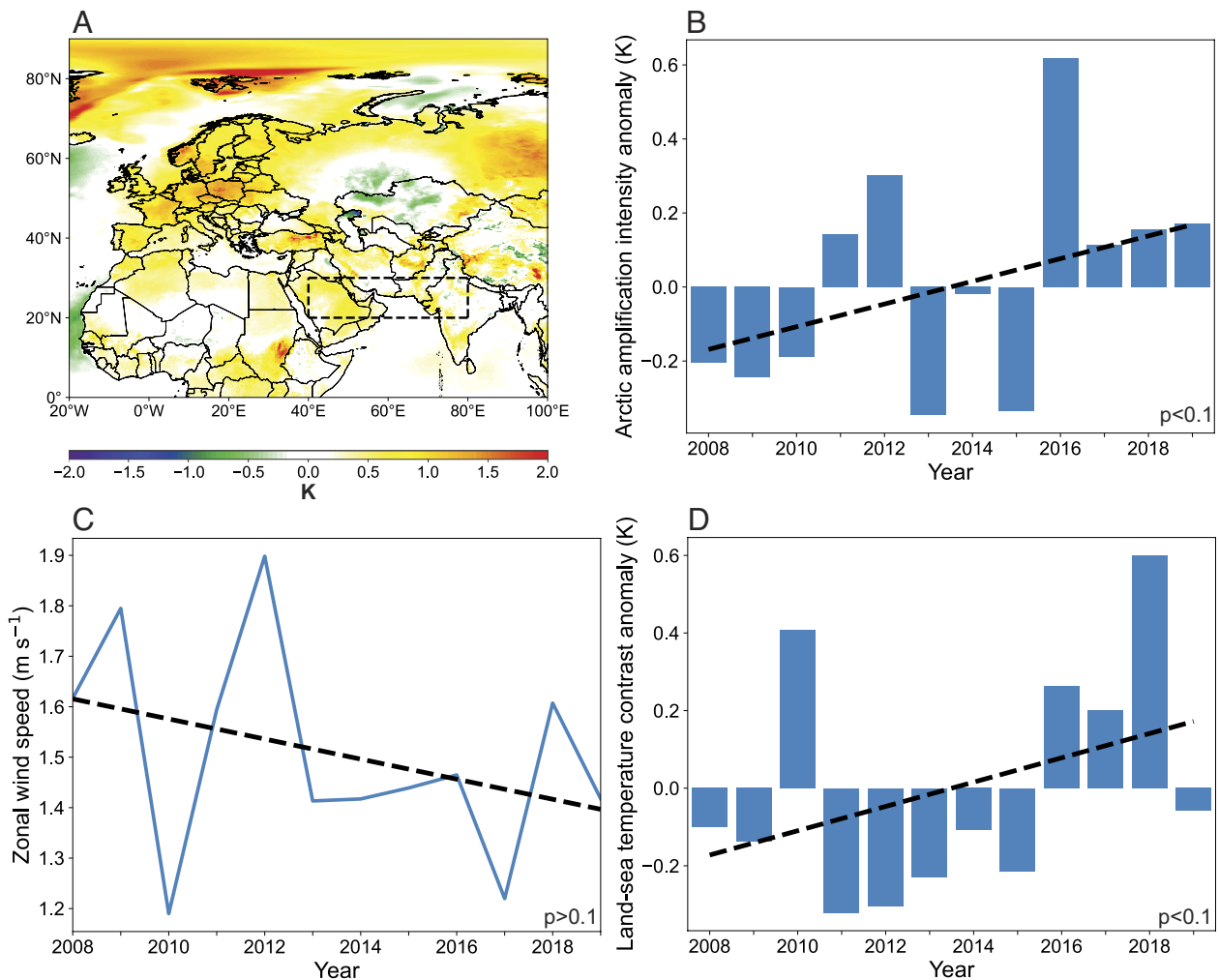
Fig. 3. Surface warming, Arctic amplification intensity, land-sea temperature contrast, and zonal wind. (*A*) Spatial distribution of surface temperature changes from Pre-period to Post-period. (*B*) Time series of Arctic amplification intensity anomalies over the 2008 to 2019 period. (*C*) Time series of averaged zonal wind at 850 hPa over the 2008 to 2019 period in the main dust transport region of West and South Asia (20°N to 30°N, 40°E to 70°E, black dashed square in *A*). (*D*) Time series of land-sea temperature contrast over the 2008 to 2019 period. Land areas and sea areas are delineated in Fig. 1 *A* and *B*.

Arctic amplification affects atmospheric circulation, which consequently regulates dust transport. In the upper atmosphere, Arctic amplification weakens the polar jet stream by reducing the thermal contrast between the Arctic and mid-latitudes, favoring larger amplitude planetary (Rossby) waves (66, 67). This allows cold polar air to move further south, bringing disturbances to the mid-latitude atmospheric circulation (43). To verify the impacts of Arctic amplification on dust activities in India and its source regions, we show the differences in large-scale atmospheric circulation between the Pre-period and the Post-period (Fig. 4). We observe a cooling in surface temperature in West Siberia (Fig. 3*A*), which corresponds to decreased pressure level in the upper atmosphere, generating a deepened trough stretching from West Siberia to Northeast India (Fig. 4*A*). Northwesterly winds behind the trough bring cold air from high-latitude regions, leading to elevated pressure in the lower atmosphere (see the purple line in Fig. 4*B*). As a result, easterly and southeasterly wind anomalies are found over the Middle East, South Asia and the Indian Ocean, which reduce dust transport from Northeast Africa to the Middle East and further to the Indian subcontinent (Fig. 4*B*). The zonal mean wind from 20°N to 30°N indicates easterly wind anomalies throughout the lower troposphere (Fig. 4*C*). Particularly at the surface level, we also observe a decreasing trend of zonal wind in

the main dust transport region of West and South Asia (Fig. 3*C*), which is also coupled with the regional land-sea warming contrast. Compared with sea surface temperatures in the Arabian Sea, the land surface temperature of the Arabian Peninsula exhibits a significantly higher increase (Fig. 3*A*). The land-sea temperature contrast defined as surface temperature difference between the Arabian Peninsula and the Arabian Sea shows an increasing trend (Fig. 3*D*). This regional warming disparity leads to an intensified sea-breeze-like circulation, partially contributing to the easterly wind anomaly and effectively suppressing the transport of dust from the Middle East to South Asia.

Apart from transport processes, anomalies in atmospheric circulation can also disrupt hydrological cycles and surface winds, therefore modifying dust emission and deposition processes in West and South Asia. The spatial distribution of dust emission index (DEI) over the period of 2008 to 2019 shows that dust emissions are more intense in the Thar Desert, Middle East, and North Africa (*SI Appendix*, Fig. S3*A*), in line with previous studies (68, 69). DEI generally decreases in West and South Asia, particularly in the Middle East and border regions of India and Pakistan (*SI Appendix*, Fig. S3*B*). Dust emissions in these arid and semi-arid regions are predominantly influenced by soil wetness, surface wind speed and vegetation coverage (24, 70). Dust emission in the Middle East is
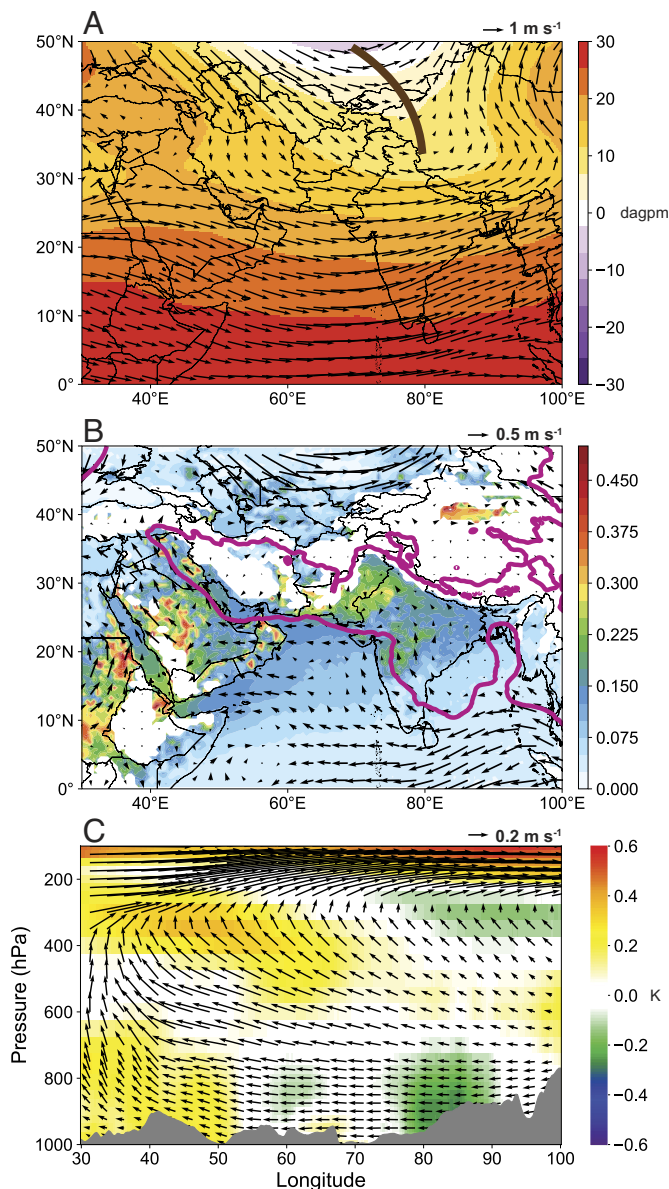
Fig. 4. Spatial distribution of changes in geopotential height, atmospheric circulation, and temperature. (*A*) Spatial distribution of geopotential height and wind changes at 100 hPa. The brown line represents the location of trough. (*B*) Spatial distribution of averaged DOD over the 2008 to 2019 period and wind changes at 850 hPa. The climatology of wind vectors is shown in *SI Appendix,* Fig. S1B. Purple lines indicate increased geopotential height of 8 dagpm at 850 hPa. (*C*) Changes of zonal mean air temperature and wind from 20°N to 30°N (as in the box of Fig. 3*A*). Vertical velocity is amplified by a factor of 10 for clarity.

the major dust source of this region (*SI Appendix,* Fig. S4A) because of low soil water content (*SI Appendix,* Fig. S4B) and high surface winds (*SI Appendix,* Fig. S4C) in the Arabian peninsula. The same conditions are also observed in border regions of India and Pakistan (*SI Appendix,* Fig. S5). Here we show that there is an increased normalized difference vegetation index (NDVI), elevated soil moisture, and weakened 10 m wind speeds around the Persian Gulf (*SI Appendix,* Fig. S6 B–D), contributing to a remarkable decrease in dust emissions in this region (*SI Appendix,* Fig. S6A). Similarly, we find that soil moisture increases and 10 m wind speed decreases in border regions in northeastern India (*SI Appendix,* Fig. S6 F and G). However, these changes are comparatively less significant than those observed in the Middle East. The combination of enhanced soil wetness and weakened surface wind in these regions suppresses

the amount of potential dust that can be emitted into the atmosphere, contributing to the lower dust loading observed during the Post-period.

We also detect enhanced precipitation over certain parts of the oceans surrounding the Middle East and South Asian subcontinent (*SI Appendix,* Fig. S7 A and D), contributing to a stronger deposition. Southeasterly wind anomalies bring abundant moisture from the Indian Ocean to the Middle East (*SI Appendix,* Fig. S7B), accompanied by enhanced vertical velocity (*SI Appendix,* Fig. S7C), causing a remarkable enhancement in precipitation in this region (*SI Appendix,* Fig. S7A). The changes in both sources and sinks, accompanied by a decline in remote transport, lead to a more significant decline in DOD over the oceans (Fig. 1*F*). We selected three sections in this region in Fig. 5*A*, denoted as section S1 (15° to 35°N, 40°E), S2 (15° to 35°N, 62°E) and S3 (15° to 35°N, 73°E), to quantify anomalies of dust flux transported to the Middle East and South Asia over the 2008 to 2019 period. Dust transport fluxes at these three sections mostly display negative anomalies during the Post-period (Fig. 5 *B–D*).

Attribution Analysis of DOD Decline. While the changes of dust loading and its transport and emissions (both in terms of linear trend during the entire period, as well as the epoch difference between the Pre-period and the Post-period) are consistent with the AAI trend and the diagnosed trends of circulation and regional climate, we further verify the causality by attribution analysis based on CMIP6 model experiments. GHG-only forcing simulations show consistent decreasing trend of dust loading in West and South Asia, while aerosols-only and land use-only forcings simulations produce increased dust in West Asia (*SI Appendix,* Fig. S8). As limited models in CMIP6 provide dust loading output and substantial uncertainties remain in modeling dust processes (71), we opt to compare the ensemble mean atmospheric circulation and surface meteorological conditions with observed patterns to strengthen the attribution. The historical and GHG-only model results are consistent, and both are in good agreement with the circulation changes shown in the reanalysis from the Pre-period to the Post-period with respect to geopotential height and wind patterns (Fig. 6 *A–D*). AAI derived from historical and GHG-only simulation also show similar trends with the ERA5 reanalysis during the period of 2008 to 2019 (*SI Appendix,* Fig. S9). Note the main troughs shown in Fig. 6 *A* and *C* are in similar locations as in the reanalysis. Correspondingly, the lower atmospheric circulation over West and South Asia exhibits an easterly wind anomaly (Fig. 6 *B* and *D*). Elevated soil moisture and weakened surface wind speeds around the Persian Gulf and in border regions of northeastern India are also detected from GHG-only model results (*SI Appendix,* Figs. S10 A and D and S11 A and D). The aerosols-only simulations exhibit different patterns of geopotential height and circulation in both the upper and lower layers (Fig. 6 *E* and *F*), which do not resemble the diagnosed main circulation patterns that drive dust changes. Furthermore, even with reduced surface wind speeds, soil moisture exhibits opposite changes to the patterns in reanalysis data in West Asia and border regions of India and Pakistan (*SI Appendix,* Figs. S10 B and E and S11 B and E).

Previous studies highlighted the contributions of local land use changes to the decline of dust loading in West and South Asia (47, 49), and here we also evaluate the response of dust loading to the land use-only forcing. As the land use forcing simulations were only extended to 2014, we conducted a similar analysis from 2008 to 2014 with the results obtained from historical simulations covering the same period (*SI Appendix,* Fig. S12). Land use forcing induces an unfavorable atmospheric circulation condition for
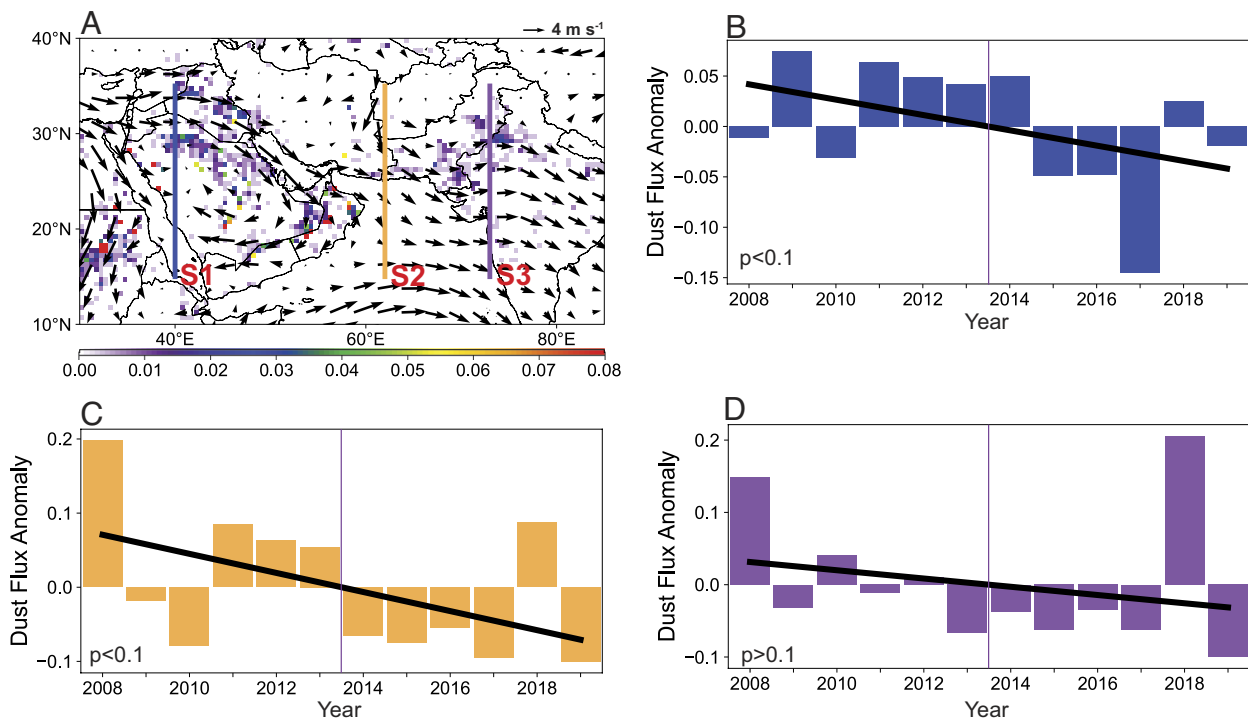
Fig. 5. Annual dust flux anomalies. (*A*) DEI, atmospheric circulation at 850 hPa and locations of three sections (blue line S1: 15° to 35°N, 40°E, yellow line S2: 15° to 35°N, 62°E and purple line S3: 15° to 35°N, 73°E). Vertically integrated dust flux anomalies at section (*B*) S1, (*C*) S2 and (*D*) S3.

declining dust loading over West and South Asia, which is not in line with the patterns observed in both reanalysis and historical simulations. Soil moisture and surface wind speeds from land use-only model results also show inconsistency with patterns in reanalysis data (*SI Appendix*, Figs. S10 *C* and *F* and S11 *C* and *F*).

Responses of dust loading in West and South Asia to an extreme CO_2 concentration enhancement are also evaluated to further support our primary conclusion of attributing DOD decline in these regions to Arctic amplification. Average dust loading over West and South Asia during the longer period of 1979 to 2014 decreases when CO_2 concentrations are four times higher than the historical values, particularly in South Asia (*SI Appendix*, Fig. S13A). The annual load of dust over West and South Asia is consistently lower in most years during this period (*SI Appendix*, Fig. S13B), with decreased zonal wind anomaly (*SI Appendix*, Fig. S13C) caused by consistently increased AAI (*SI Appendix*, Fig. S13B) and land-sea temperature contrast (*SI Appendix*, Fig. S13C). Large-scale atmospheric circulation also shows a similar weaker low-pressure center over West Siberian in the upper atmosphere and a high-pressure center over the Iranian Plateau in the lower atmosphere (*SI Appendix*, Fig. S13 *E* and *F*), creating easterly wind anomalies that inhibit dust transport from the Middle East to South Asia.

Discussion

While some previous studies demonstrated the influence of land management practices on dust loading reduction in West and South Asia (44, 46, 47, 49), our research provides an additional dimension to this understanding by shedding light on the role of climate change-induced alterations in atmospheric circulation. Undoubtedly local land management remains a vital contributor to dust loading dynamics, and our findings, by showing the indirect effect of circulation on local rainfall and soil moisture, corroborate the efficacy of sustained vegetation expansion in mitigating dust emissions. However, the insight from our analysis is the increasingly dominant influence of circulation change on the broader global climate context. Changes in atmospheric circulation patterns, driven by global climate dynamics shifts, have emerged as the principal driver behind the observed recent dust reductions in West and South Asia. Similar results, that emphasize the dominant role of changes in atmospheric circulation apart from local land management, have also been detected in other dust-vulnerable regions of the world such as East Asia (72–74), North Africa (75, 76), and West Australia (77, 78).

Since dust aerosols are net climate coolers, we used CMIP6 simulation outputs and conducted Community Earth System Model (CESM) simulations to explain how declining dust affects temperature and AAI. We find that reduced aerosols cause warming in mid-latitudes of the northern hemisphere but create less influences on the Arctic (*SI Appendix*, Fig. S14A), which decreases AAI from 2008 to 2019 (*SI Appendix*, Fig. S14B). Our CESM simulations also confirm that radiative effects of dust are limited to high dust loading areas (*SI Appendix*, Fig. S15), suggesting that declines in dust in West and South Asia might not affect Arctic warming to enhance AAI. This feedback is masked by continuously increasing amount of GHGs. The decreasing dust loading in West and South Asia may be considered as a positive trend, but it still underscores the ongoing need to address dust issues in this region. The shift in dust loading caused by Arctic amplification under the background of global warming in recent years provides hints on potentially negative impacts on the environment in West and South Asia with global efforts to curb future warming (*SI Appendix*, Fig. S16). Dust loading declines after 2020 under the high warming SSP585 scenario at the end of 21st century due to higher GHG levels (*SI Appendix*, Fig. S16). However, dust loading over West and South Asia is projected to decrease until around 2050 and then increase toward the end of this century under the SSP126 scenario (*SI Appendix*, Fig. S16), which is highly associated with changes in GHG emissions under this scenario (63). Overall, the dust loadings in the cleaner SSP126
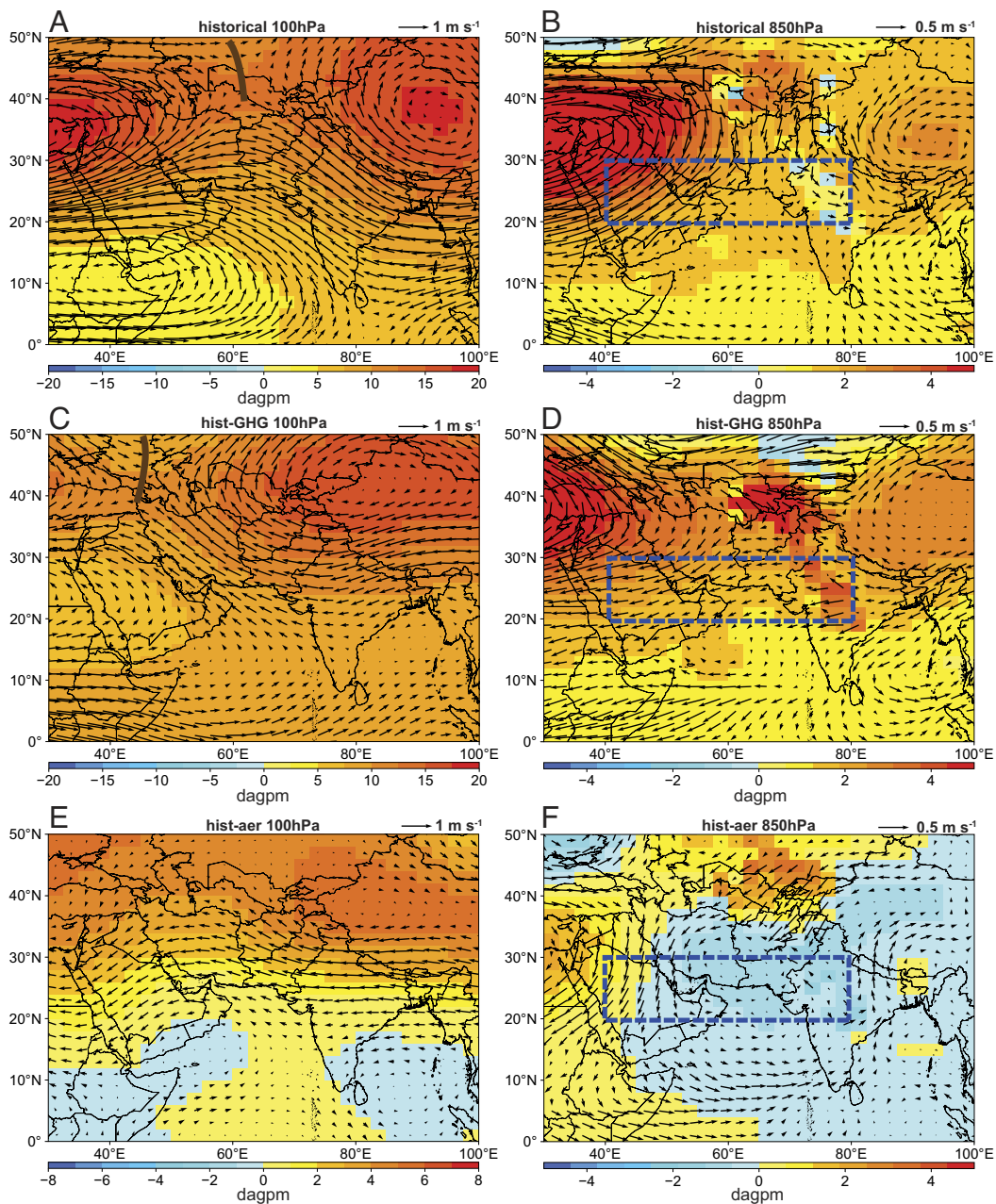
Fig. 6. Spatial distribution of geopotential height and atmospheric circulation changes. Spatial distribution of changes in geopotential height and wind from the Pre-period to the Post-period in West and South Asia at (*A*) 100 hPa and (*B*) 850 hPa from historical all forcing experiments. (*C*) and (*D*) are from GHG-only forcing experiments. (*E*) and (*F*) are from aerosols-only forcing experiments.

scenario which reaches carbon neutrality by mid-century is higher than SSP585 projection by at least 10% in 2100 s.

These model projections suggest a possible increase in dust loading in West and South Asia under a global "sustainability" scenario with anthropogenic radiative forcing decreasing in the future. Therefore, we argue that in addition to controlling GHG emissions, more local efforts need to be devoted to countering desertification in West and South Asia to reduce potential natural dust emissions. In arid and semi-arid regions, continued deserti-fication due to human activities could worsen airborne dust level, even when weather conditions are not conducive for dust emission (79, 80). Although natural sources contribute more significantly to total dust loading, rapid urbanization, and industrialization, along with increased construction activities, road dust, and vehic-ular emissions, also contributed to high levels of anthropogenic

dust emissions in West and South Asia in recent decades (81, 82). Recent declines in total DOD did not necessarily imply an improved surface air quality in the future, and more attention is still needed to monitor urban-level dust concentration.

Besides, a decrease in dust load may contribute positively to dust exposure and respiratory health; it could also result in increased warming over the coming critical decades (83, 84). Partly due to the continuous decline in dust loading under the SSP585 scenario, the surface temperature of West and South Asia tends to increase at a faster rate in the later years of 21st century, and the temperature differences can reach as high as ~0.4 °C (*SI Appendix,* Fig. S17*A*). While with high dust aerosol under the SSP126 sce-nario, surface temperature of West and South Asia are generally lower than the global mean (*SI Appendix,* Fig. S17*B*). Debnath et al. (85) concluded that 30% to 60% decrease in dust loading

over West and South Asia in June–July–August–September season of 2017 led to 15 to 30 W m^{-2} increase in clear-sky surface net radiation. Asutosh et al. (46) reported that the 17% decline in DOD over the North-Western part of India from 2001 to 2015 led to increases in the top and bottom of the atmosphere shortwave radiative forcing (7 and 11.6%, respectively), but an overall decline in the atmospheric heating and atmospheric radiative forcing (~16%). Based on our CESM2 simulation results, annual average surface air temperature in West and South Asia increases about 0.15 °C in 2008 if dust loading declines to zero. All these results suggest that residents in West and South Asia are likely to experience higher temperature if the declining trend persists. Such an increase in temperature due to declining dust could amplify health harms under the context of rapid ongoing urbanization and increasing GHGs.

Materials and Methods

Satellite Retrievals and Reanalysis Data. Daily gridded 10 μm DOD and dust layer height at 9:30 am and 9:30 pm from January 2008 to December 2019 were obtained from the IASI level 2 product (https://iasi.aeris-data.fr/). The spatial resolution used in this study was 0.5° × 0.5°. IASI is a high-resolution infrared sounder instrument launched onboard the European Meteorological Operational satellite (METOP) to measure the Earth's atmosphere infrared radiation (86). IASI provides global retrievals of DOD and dust layer height at infrared bands, showing high quality in capturing the spatiotemporal variability of dust in comparison to ground measurements from the AERONET (53, 54). We calculated DOD anomalies by subtracting average DOD over the whole study period of 2008 to 2019.

In this study, we used the combined Dark Target/Deep Blue (DT/DB) AOD product (87, 88), an integral component of the MODIS-Aqua Collection 061 (MYD04-C061) dataset from May to July for the period of 2003 to 2019. The data were at 10 km × 10 km resolution but were regridded onto a 0.25° × 0.25° uniform grid on a daily basis. Specifically, the AOD product at 0.55 μm obtained from the Aqua satellite was used for the present work. AOD retrieval over land is facilitated by two distinct operational algorithms: the Dark-Target (DT) algorithm, optimized for vegetated land surfaces (87), and the deep blue (DB) algorithm, designed for use over bright surfaces such as arid and desert regions (89). The best quality AOD retrievals with Quality Assurance (QA) value of 3 were used to ensure stringent cloud filtering.

The DOD was also obtained from CALIOP onboard Cloud-Aerosol Lidar and Infrared Pathfinder Satellite Observations (CALIPSO) for the period of 2007 to 2019. Specifically, we employed Level 3 tropospheric aerosol profile cloud-free version 4.21 product to construct monthly mean dust AOD across a consistent spatial grid within the troposphere. The estimation of DOD in level 3 data product was derived by analyzing level 2 dust extinction profiles over a uniform spatial grid (2° latitude × 5° longitude) throughout the troposphere, reaching an altitude of 12 km. The creation of Level 3 datasets involved a systematic evaluation of atmospheric conditions, encompassing both sky conditions and lightning events, and was conducted on a monthly basis.

We also used the CALIOP-based level 2 version 4.20 standard aerosol profile products (vertical and horizontal resolution: 60 m × 5 km, temporal resolution: 5.92 s) to examine the vertical distribution of dust aerosols. We obtained extinction coefficient at 532 nm and aerosol subtypes for the present study. The hybrid extinction retrieval algorithms were used to retrieve aerosol extinction profiles, using the assumed lidar ratios appropriate for each aerosol type (90, 91). In the present study, we segregated aerosol signals based on the "CAD (Cloud-Aerosol Discrimination) score" given in CALIPSO profile products (92, 93). The sign and absolute value of the CAD score determined the object type (positive: cloud; negative: aerosol) and the confidence level of the classification. We selected aerosol signals with CAD score less than −70 for the present study (94). Additionally, aerosol profiles with extinction QC (Quality Control) flags of 0 and 1 were considered in the analysis, which help to reduce some large errors due to the non-linear behavior of the AOD retrievals (95). The DOF was calculated by dividing the total number of dust samples by the total number of CALIPSO measurements. The percentage change in DOF was the difference of DOF between the first three

consecutive years (2007 to 2009) and the last three consecutive years (2017 to 2019) over the Middle East region. The daily version 3 level 2 spectral deconvolution algorithm (SDA) retrieval of total and coarse mode AOD at 500 nm from AERONET over 2008 to 2019 was also used in this study. It is a quality-assured product with pre- and post-field calibration applied (automatically cloud cleared and manually inspected). We only selected sites with over 75% data coverage in each year during the study period of 2008 to 2019.

The monthly Level 3 global NDVI was retrieved by the MODIS instrument aboard the Terra satellite. The spatial resolution of this dataset was 1 km × 1 km. Meteorological variables including monthly gridded surface temperature, 10-m wind speed, geopotential height and u- and v-components of wind at various layers (100, 200, 850 hPa), vertical velocity at 500 hPa, total precipitation, vertical integrated moisture divergence were taken from the European Centre for Medium-Range Weather Forecasts (ECMWF) Reanalysis version 5 (ERA5) dataset (96). The spatial resolution of all these variables was 0.25° × 0.25°.

Climate Model Outputs. The historical simulations driven by time evolving single forcing of GHG-only and aerosols-only from the detection and attribution model intercomparison project (DAMIP) in CMIP6 were employed in this study to evaluate climate response to individual forcings (97). We compared monthly gridded dust loading, geopotential heights, zonal and meridional winds, surface temperature, surface wind speed and soil moisture with observations to test attribution hypothesis. To cover the study period spanning from 2008 to 2019, following previous studies (98, 99), historical simulations were extended for 2015 to 2019 using corresponding SSP245 scenario simulations as GHG-only and aerosols-only simulations for 2015 to 2020 follow the SSP245 scenario (97). We only adopted outputs from 2008 to 2014 in land use-only simulation because of data limitation. When multiple runs were available from a model, we utilized only the first run to ensure equal weighting for each model in this analysis. The model output was interpolated to 2° × 2.5° grids before further analysis. The list of selected models is shown in *SI Appendix*, Tables S1−S3.

We compared monthly gridded outputs of the historical atmospheric model intercomparison project (AMIP) and the AMIP-4 × CO_2 experiments in CMIP6 to evaluate and quantify the impacts of CO_2-induced climate change on dust loading in West and South Asia. The AMIP experiment uses observed sea surface temperatures and sea ice concentrations as boundary conditions, while allowing the atmosphere to freely evolve. The AMIP-4 × CO_2 was identical to the AMIP, except that the CO_2 concentrations were set at four times the AMIP concentrations (100). Selected variables in the analysis include loads of dust, surface temperature, geopotential heights, and zonal and meridional winds. The simulation period was 1979 to 2014 and the model output was also interpolated to 2° × 2.5° grids. The list of selected models is shown in *SI Appendix*, Table S4.

We also analyzed dust loadings over the period of 2020 to 2100 under the SSP126 and SSP585 scenarios from CMIP6 to determine future shift of dust loading in West and South Asia under high and low GHG emission scenarios. SSP126 is a Sustainability pathway that follows low carbon development, but SSP585 is a "Fossil-Fueled Development" pathway that assumes a heavy reliance on fossil fuels and a slow transition to low-carbon energy sources (101, 102). We used bilinear interpolation to regrid model outputs onto 2° × 2.5° grids and calculated average dust loading under both SSP126 and SSP585 scenarios. The list of selected models is shown in *SI Appendix*, Table S5.

Dust Emission Index and Dust Horizontal Transport Flux. Following Chédin et al. (103), we defined monthly dust emission index (DEI) as the frequency of occurrence, normalized by the proportion of cases observed with simultaneous high DOD (≥0.5) and low dust layer mean altitude (≤1.1 km), because this simultaneous occurrence helps distinguish newly emitted dust from the aged dust transported at higher levels. To quantify horizontal transport of dust, we adopted the approach of Yu et al. (40) and developed an approximate estimation of dust flux in the zonal direction by combining averaged zonal wind (from ERA5) beneath the dust layer height (from IASI) with total IASI DOD since we have limited information of vertical profiles of dust mass.

CESM Experiment. CESM v2.1.3 was used to explore global dust radiative effects. The chosen component set (compset) for this study was FWHIST, the robustness of which has undergone extensive validation (103). Detailed settings

of FWHIST can be found in our previous study (104), and here we incorporated a diagnostic calculation to quantify dust radiative influences by turning off dust radiative effect in CESM.

Data, Materials, and Software Availability. All study data are included in the article and/or SI Appendix.

Author affiliations: [a]Department of Geography, Hong Kong Baptist University, Hong Kong SAR 999077, China; [b]John A. Paulson School of Engineering and Applied Sciences, Harvard University, Cambridge, MA 02138; [c]Department of Atmospheric Sciences, Texas A&M University, College Station, TX 77843; [d]Environmental Defense Fund, Washington, DC 20009; [e]Jet Propulsion Laboratory, California Institute of Technology, Pasadena, CA 91109; [f]Oak Ridge Associated Universities, Oak Ridge, TN 37830; [g]Department of Precision Machinery and Precision Instrumentation, University of Science and Technology of China, Hefei 230026, China; [h]Key Laboratory of Environmental Optics and Technology, Anhui Institute of Optics and Fine Mechanics, Hefei Institutes of Physical Science, Chinese Academy of Sciences, Hefei 230031, China; [i]National Climate Center, Chinese Meteorological Administration, Beijing 100081, China; [j]Collaborative Innovation Center on Forecast and Evaluation of Meteorological Disasters, School of Atmospheric Physics, Nanjing University of Information Science and Technology, Nanjing 210044, China; [k]Department of Geography and Institute for Climate and Carbon Neutrality, The University of Hong Kong, Hong Kong SAR 999077, China; and [l]Department of Chemical and Biochemical Engineering, The University of Iowa, Iowa City, IA 52242

1. P. Ginoux et al., Sources and distributions of dust aerosols simulated with the GOCART model. *J. Geophys. Res. Atmos.* **106**, 20255–20273 (2001).
2. C. Textor et al., Analysis and quantification of the diversities of aerosol life cycles within AeroCom. *Atmos. Chem. Phys.* **6**, 1777–1813 (2006).
3. B. Fubini, C. O. Arean, Chemical aspects of the toxicity of inhaled mineral dusts. *Chem. Soc. Rev.* **28**, 373–381 (1999).
4. G. Shi et al., Potentially toxic metal contamination of urban soils and roadside dust in Shanghai, China. *Environ. Pollut.* **156**, 251–260 (2008).
5. D. Q. Tong et al., Dust storms, valley fever, and public awareness. *GeoHealth* **6**, e2022GH000642 (2022).
6. N. M. Mahowald et al., Observed 20th century desert dust variability: Impact on climate and biogeochemistry. *Atmos. Chem. Phys.* **10**, 10875–10893 (2010).
7. R. Gautam, Z. Liu, R. P. Singh, N. C. Hsu, Two contrasting dust-dominant periods over India observed from MODIS and CALIPSO data. *Geophys. Res. Lett.* **36**, L06813 (2009).
8. G. Pandithurai et al., Aerosol radiative forcing during dust events over New Delhi, India. *J. Geophys. Res. Atmos.* **113**, D13209 (2008).
9. R. P. Singh, S. Dey, S. N. Tripathi, V. Tare, B. Holben, Variability of aerosol parameters over Kanpur, Northern India. *J. Geophys. Res. Atmos.* **109**, D23206 (2004).
10. A. S. Goudie, Desert dust and human health disorders. *Environ. Int.* **63**, 101–113 (2014).
11. P. J. Gregory, J. S. Ingram, M. Brklacich, Climate change and food security. *Philos. Trans. R. Soc. B: Biol. Sci.* **360**, 2139–2148 (2005).
12. B. Prusty, P. Mishra, P. Azeez, Dust accumulation and leaf pigment content in vegetation near the national highway at Sambalpur, Orissa, India. *Ecotoxicol. Environ. Safety* **60**, 228–235 (2005).
13. S. Sarkar, A. Chauhan, R. Kumar, R. P. Singh, Impact of deadly dust storms (May 2018) on air quality, meteorological, and atmospheric parameters over the northern parts of India. *GeoHealth* **3**, 67–80 (2019).
14. UN ESCAP, Sand and dust storms risk assessment in Asia and the Pacific. https://hdl.handle.net/20.500.12870/4452 (2021). Accessed 6 March 2024.
15. D. Giannadaki, A. Pozzer, J. Lelieveld, Modeled global effects of airborne desert dust on air quality and premature mortality. *Atmos. Chem. Phys.* **14**, 957–968 (2014).
16. D. J. Cziczo et al., Clarifying the dominant sources and mechanisms of cirrus cloud formation. *Science* **340**, 1320–1324 (2013).
17. K. D. Froyd et al., Dominant role of mineral dust in cirrus cloud formation revealed by global-scale measurements. *Nat. Geosci.* **15**, 177–183 (2022).
18. J. F. Kok et al., Smaller desert dust cooling effect estimated from analysis of dust size and abundance. *Nat. Geosci.* **10**, 274–278 (2017).
19. J. F. Kok et al., Mineral dust aerosol impacts on global climate and climate change. *Nat. Rev. Earth Environ.* **4**, 71–86 (2023).
20. J. A. Cruz, F. McDermott, M. J. Turrero, R. L. Edwards, J. Martín-Chivelet, Strong links between Saharan dust fluxes, monsoon strength, and North Atlantic climate during the last 5000 years. *Sci. Adv.* **7**, eabe6102 (2021).
21. G. Nandini, V. Vinoj, S. K. Pandey, Arabian sea aerosol-Indian summer monsoon rainfall relationship and its modulation by El-Nino Southern Oscillation. *npj Clim. Atmos. Sci.* **5**, 25 (2022).
22. V. Vinoj et al., Short-term modulation of Indian summer monsoon rainfall by West Asian dust. *Nat. Geosci.* **7**, 308–313 (2014).
23. P. Banerjee, S. K. Satheesh, K. K. Moorthy, R. S. Nanjundiah, V. S. Nair, Long-range transport of mineral dust to the Northeast Indian Ocean: Regional versus remote sources and the implications. *J. Clim.* **32**, 1525–1549 (2019).
24. P. Ginoux, J. M. Prospero, T. E. Gill, N. C. Hsu, M. Zhao, Global-scale attribution of anthropogenic and natural dust sources and their emission rates based on MODIS Deep Blue aerosol products. *Rev. Geophys.* **50**, RG3005 (2012).
25. L. Shi, J. Zhang, F. Yao, D. Zhang, H. Guo, Drivers to dust emissions over dust belt from 1980 to 2018 and their variation in two global warming phases. *Sci. Total Environ.* **767**, 144860 (2021).
26. H. Cao, F. Amiraslani, J. Liu, N. Zhou, Identification of dust storm source areas in West Asia using multiple environmental datasets. *Sci. Total Environ.* **502**, 224–235 (2015).
27. H. Gandham, H. P. Dasari, A. Karumuri, P. M. K. Ravuri, I. Hoteit, Three-dimensional structure and transport pathways of dust aerosols over West Asia. *npj Clim. Atmos. Sci.* **5**, 45 (2022).
28. T. Y. Tanaka, M. Chiba, A numerical study of the contributions of dust source regions to the global dust budget. *Glob. Planet. Change* **52**, 88–104 (2006).
29. K. V. S. Badarinath et al., Long-range transport of dust aerosols over the Arabian Sea and Indian region–A case study using satellite data and ground-based measurements. *Glob. Planet. Change* **72**, 164–181 (2010).
30. P. Banerjee, S. K. Satheesh, K. K. Moorthy, The unusual severe dust storm of May 2018 over Northern India: Genesis, propagation, and associated conditions. *J. Geophys. Res. Atmos.* **126**, e2020JD032369 (2021).
31. D. Kaskaoutis et al., Assessment of changes in atmospheric dynamics and dust activity over southwest Asia using the Caspian Sea-Hindu Kush Index. *Int. J. Climatol.* **37**, 1013–1034 (2017).
32. I. Mattis, A. Ansmann, D. Müller, U. Wandinger, D. Althausen, Dual-wavelength Raman lidar observations of the extinction-to-backscatter ratio of Saharan dust. *Geophys. Res. Lett.* **29**, 20-21–20-24 (2002).
33. Y. Dai et al., Stratospheric impacts on dust transport and air pollution in West Africa and the Eastern Mediterranean. *Nat. Commun.* **13**, 7744 (2022).
34. Y. Shao, M. Klose, K.-H. Wyrwoll, Recent global dust trend and connections to climate forcing. *J. Geophys. Res. Atmos.* **118**, 11107–11118 (2013).
35. G. Wu et al., Tibetan Plateau climate dynamics: Recent research progress and outlook. *Natl. Sci. Rev.* **2**, 100–116 (2015).
36. Y. Yu et al., Assessing temporal and spatial variations in atmospheric dust over Saudi Arabia through satellite, radiometric, and station data. *J. Geophys. Res. Atmos.* **118**, 13253–13264 (2013).
37. D. G. Kaskaoutis et al., Influence of anomalous dry conditions on aerosols over India: Transport, distribution and properties. *J. Geophys. Res. Atmos.* **117**, D09106 (2012).
38. N. K. Lodhi, S. N. Beegum, S. Singh, K. Kumar, Aerosol climatology at Delhi in the western Indo-Gangetic Plain: Microphysics, long-term trends, and source strengths. *J. Geophys. Res. Atmos.* **118**, 1361–1375 (2013).
39. L. Wei et al., Black carbon–climate interactions regulate dust burdens over India revealed during COVID-19. *Nat. Commun.* **13**, 1839 (2022).
40. H. Yu et al., Quantification of trans-Atlantic dust transport from seven-year (2007–2013) record of CALIPSO lidar measurements. *Remote Sens. Environ.* **159**, 232–249 (2015).
41. T. J. Crowley, R. A. Berner, CO_2 and climate change. *Science* **292**, 870–872 (2001).
42. S. A. Montzka, E. J. Dlugokencky, J. H. Butler, Non-CO_2 greenhouse gases and climate change. *Nature* **476**, 43–50 (2011).
43. J. Cohen et al., Recent Arctic amplification and extreme mid-latitude weather. *Nat. Geosci.* **7**, 627–637 (2014).
44. S. K. Pandey, V. Vinoj, K. Landu, S. S. Babu, Declining pre-monsoon dust loading over South Asia: Signature of a changing regional climate. *Sci. Rep.* **7**, 16062 (2017).
45. A. G. Turner, H. Annamalai, Climate change and the South Asian summer monsoon. *Nat. Clim. Change* **2**, 587–595 (2012).
46. A. Asutosh, S. Pandey, V. Vinoj, R. Ramisetty, N. Mittal, Assessment of recent changes in dust over South Asia using RegCM4 regional climate model. *Remote Sens.* **13**, 4309 (2021).
47. Q. Jin, C. Wang, The greening of Northwest Indian subcontinent and reduction of dust abundance resulting from Indian summer monsoon revival. *Sci. Rep.* **8**, 4573 (2018).
48. E. Proestakis et al., Nine-year spatial and temporal evolution of desert dust aerosols over South and East Asia as revealed by CALIOP. *Atmos. Chem. Phys.* **18**, 1337–1362 (2018).
49. W. Xia, Y. Wang, B. Wang, Decreasing dust over the Middle East partly caused by irrigation expansion. *Earth's Future* **10**, e2021EF002252 (2022).
50. M. Nazish Khan, M. Sajid Akhter, Spatial variability and trend analysis of dust aerosols loading over Indian sub-continent using MERRA 2 & CALIPSO data. *Geol. Ecol. Landscapes*, 1–9 (2022).
51. N. B. Lakshmi, S. S. Babu, V. S. Nair, Recent regime shifts in mineral dust trends over South Asia from long-term CALIPSO observations. *IEEE Trans. Geosci. Remote Sens.* **57**, 4485–4489 (2019).
52. Y. Yang et al., Fast climate responses to aerosol emission reductions during the COVID-19 pandemic. *Geophys. Res. Lett.* **47**, e2020GL089788 (2020).
53. V. Capelle et al., Infrared dust aerosol optical depth retrieved daily from IASI and comparison with AERONET over the period 2007–2016. *Remote Sens. Environ.* **206**, 15–32 (2018).
54. V. Capelle et al., Evaluation of IASI-derived dust aerosol characteristics over the tropical belt. *Atmos. Chem. Phys.* **14**, 9343–9362 (2014).
55. R. Levy, C. Hsu, MODIS atmosphere L2 aerosol product. NASA MODIS adaptive processing system. https://doi.org/10.5067/MODIS/MOD04_L2.061 (2015). Accessed 6 March 2024.
56. D. M. Winker, W. H. Hunt, C. A. Hostetler, "Status and performance of the CALIOP lidar" in Laser Radar Techniques for Atmospheric Sensing (SPIE, 2004), pp. 8–15.
57. D. M. Winker, W. H. Hunt, M. J. McGill, Initial performance assessment of CALIOP. *Geophys. Res. Lett.* **34**, L19803 (2007).
58. J. Z. Tindan, Q. Jin, B. Pu, Understanding day–night differences in dust aerosols over the dust belt of North Africa, the Middle East, and Asia. *Atmos. Chem. Phys.* **23**, 5435–5466 (2023).
59. M. C. Serreze, R. G. Barry, Processes and impacts of Arctic amplification: A research synthesis. *Glob. Planet. Change* **77**, 85–96 (2011).
60. M. Fang, X. Li, H. W. Chen, D. Chen, Arctic amplification modulated by Atlantic Multidecadal Oscillation and greenhouse forcing on multidecadal to century scales. *Nat. Commun.* **13**, 1865 (2022).
61. T. J. Ballinger et al., Surface air temperature: Arctic Report Card: Update for 2020. https://doi.org/10.25923/gcw8-2z06 (2020). Accessed 6 March 2024.
62. M. R. England, I. Eisenman, N. J. Lutsko, T. J. Wagner, The recent emergence of Arctic Amplification. *Geophys. Res. Lett.* **48**, e2021GL094086 (2021).
63. Q. You et al., Warming amplification over the Arctic Pole and Third Pole: Trends, mechanisms and consequences. *Earth-Sci. Rev.* **217**, 103625 (2021).
64. R. Zhang et al., Understanding the cold season Arctic surface warming trend in recent decades. *Geophys. Res. Lett.* **48**, e2021GL094878 (2021).
65. V. Petoukhov, S. Rahmstorf, S. Petri, H. J. Schellnhuber, Quasiresonant amplification of planetary waves and recent Northern Hemisphere weather extremes. *Proc. Natl. Acad. Sci. U.S.A.* **110**, 5336–5341 (2013).
66. J. A. Francis, S. J. Vavrus, Evidence linking Arctic amplification to extreme weather in mid-latitudes. *Geophys. Res. Lett.* **39**, L06801 (2012).

67. J. A. Screen, I. Simmonds, Amplified mid-latitude planetary waves favour particular regional weather extremes. *Nat. Clim. Change* **4**, 704–709 (2014).
68. A. Chappell *et al.*, Satellites reveal Earth's seasonally shifting dust emission sources. *Sci. Total Environ.* **883**, 163452 (2023).
69. J. F. Kok *et al.*, Contribution of the world's main dust source regions to the global cycle of desert dust. *Atmos. Chem. Phys.* **21**, 8169–8193 (2021).
70. C. Wu, Z. Lin, Y. Shao, X. Liu, Y. Li, Drivers of recent decline in dust activity over East Asia. *Nat. Commun.* **13**, 7105 (2022).
71. A. Zhao, C. L. Ryder, L. J. Wilcox, How well do the CMIP6 models simulate dust aerosols? *Atmos. Chem. Phys.* **22**, 2095–2119 (2022).
72. J. Liu *et al.*, Impact of Arctic amplification on declining spring dust events in East Asia. *Clim. Dyn.* **54**, 1913–1935 (2020).
73. R. Mao, D. Gong, J. Bao, Y. Fan, Possible influence of Arctic Oscillation on dust storm frequency in North China. *J. Geogr. Sci.* **21**, 207–218 (2011).
74. R. Mao, C.-H. Ho, Y. Shao, D.-Y. Gong, J. Kim, Influence of Arctic Oscillation on dust activity over northeast Asia. *Atmos. Environ.* **45**, 326–337 (2011).
75. C. Moulin, C. E. Lambert, F. Dulac, U. Dayan, Control of atmospheric export of dust from North Africa by the North Atlantic Oscillation. *Nature* **387**, 691–694 (1997).
76. P. Salvador *et al.*, African dust outbreaks over the western Mediterranean Basin: 11-year characterization of atmospheric circulation patterns and dust source areas. *Atmos. Chem. Phys.* **14**, 6759–6775 (2014).
77. P. De Deckker, An evaluation of Australia as a major source of dust. *Earth-Sci. Rev.* **194**, 536–567 (2019).
78. M. Ekström, G. H. McTainsh, A. Chappell, Australian dust storms: Temporal trends and relationships with synoptic pressure distributions (1960–99). *Int. J. Climatol.* **24**, 1581–1599 (2004).
79. A. Kundu, D. Dutta, Monitoring desertification risk through climate change and human interference using remote sensing and GIS techniques. *Int. J. Geomat. Geosci.* **2**, 21–33 (2011).
80. M. Mainguet, *Desertification: Natural Background and Human Mismanagement* (Springer Science & Business Media, 2012).
81. W. Xia *et al.*, Double trouble of air pollution by anthropogenic dust. *Environ. Sci. Technol.* **56**, 761–769 (2022).
82. R. Yadav, L. K. Sahu, G. Beig, N. Tripathi, S. N. A. Jaaffrey, Ambient particulate matter and carbon monoxide at an urban site of India: Influence of anthropogenic emissions and dust storms. *Environ. Pollut.* **225**, 291–303 (2017).
83. J. Lelieveld *et al.*, Effects of fossil fuel and total anthropogenic emission removal on public health and climate. *Proc. Natl. Acad. Sci. U.S.A.* **116**, 7192–7197 (2019).
84. H. Nair *et al.*, Aerosol demasking enhances climate warming over South Asia. *npj Clim. Atmos. Sci.* **6**, 39 (2023).
85. S. Debnath *et al.*, Impact of dust aerosols on the Indian Summer Monsoon Rainfall on intra-seasonal time-scale. *Atmos. Environ.* **305**, 119802 (2023).
86. D. Blumstein *et al.*, IASI instrument: Technical overview and measured performances. *Infrared Spaceborne Remote Sens. XII* **5543**, 196–207 (2004).
87. R. Levy *et al.*, The Collection 6 MODIS aerosol products over land and ocean. *Atmos. Meas. Tech.* **6**, 2989–3034 (2013).
88. A. Sayer *et al.*, MODIS Collection 6 aerosol products: Comparison between Aqua's e-Deep Blue, Dark Target, and "merged" data sets, and usage recommendations. *J. Geophys. Res. Atmos.* **119**, 13965–13989 (2014).
89. N. Hsu *et al.*, Enhanced Deep Blue aerosol retrieval algorithm: The second generation. *J. Geophys. Res. Atmos.* **118**, 9296–9315 (2013).
90. M. Vaughan *et al.*, Cloud-aerosol LIDAR infrared pathfinder satellite observations (CALIPSO)-data management system. *Data Prod. Catalog* **V4**, 95 (2023).
91. S. A. Young, M. A. Vaughan, The retrieval of profiles of particulate extinction from Cloud-Aerosol Lidar Infrared Pathfinder Satellite Observations (CALIPSO) data: Algorithm description. *J. Atmos. Oceanic Technol.* **26**, 1105–1119 (2009).
92. M. A. Vaughan *et al.*, Fully automated detection of cloud and aerosol layers in the CALIPSO lidar measurements. *J. Atmos. Oceanic Technol.* **26**, 2034–2050 (2009).
93. M. A. Vaughan *et al.*, Fully automated analysis of space-based lidar data: An overview of the CALIPSO retrieval algorithms and data products. *Laser Radar Tech. Atmos. Sens.* **5575**, 16–30 (2004).
94. J. Fuchs, J. Cermak, Where aerosols become clouds–Potential for global analysis based on CALIPSO data. *Remote Sens.* **7**, 4178–4190 (2015).
95. J. Huang *et al.*, CALIPSO inferred most probable heights of global dust and smoke layers. *J. Geophys. Res.: Atmos.* **120**, 5085–5100 (2015).
96. H. Hersbach *et al.*, The ERA5 global reanalysis. *Q. J. R. Meteorol. Soc.* **146**, 1999–2049 (2020).
97. N. P. Gillett *et al.*, The detection and attribution model intercomparison project (DAMIP v1. 0) contribution to CMIP6. *Geosci. Model Dev.* **9**, 3685–3697 (2016).
98. J. Liu *et al.*, Contributions of anthropogenic forcings to evapotranspiration changes over 1980–2020 using GLEAM and CMIP6 simulations. *J. Geophys. Res. Atmos.* **126**, e2021JD035367 (2021).
99. S. Paik, S.-K. Min, Quantifying the anthropogenic greenhouse gas contribution to the observed spring snow-cover decline using the CMIP6 multimodel ensemble. *J. Clim.* **33**, 9261–9269 (2020).
100. V. Eyring *et al.*, Overview of the Coupled Model Intercomparison Project Phase 6 (CMIP6) experimental design and organization. *Geosci. Model Dev.* **9**, 1937–1958 (2016).
101. B. C. O'Neill *et al.*, A new scenario framework for climate change research: The concept of shared socioeconomic pathways. *Clim. Change* **122**, 387–400 (2013).
102. K. Riahi *et al.*, The Shared Socioeconomic Pathways and their energy, land use, and greenhouse gas emissions implications: An overview. *Glob. Environ. Change* **42**, 153–168 (2017).
103. A. Chédin, V. Capelle, N. A. Scott, M. C. Todd, Contribution of IASI to the observation of dust aerosol emissions (morning and nighttime) over the Sahara Desert. *J. Geophys. Res. Atmos.* **125**, e2019JD032014 (2020).
104. M. Gao *et al.*, Large-scale climate patterns offer preseasonal hints on the co-occurrence of heat wave and O3 pollution in China. *Proc. Natl. Acad. Sci. U.S.A.* **120**, e2218274120 (2023).